Topological Characterization and Uncertainty Visualization of Atmospheric Rivers

Fangfei Lan[1] , Brandi Gamelin[2] , Lin Yan[3] , Jiali Wang[2] , Bei Wang[1] , Hanqi Guo[4]

[1]Scientific Computing and Imaging Institute, University of Utah, USA
[2]Environmental Science Division, Argonne National Laboratory, IL, USA
[3]Department of Computer Science, Iowa State University, USA
[4]Department of Computer Science and Engineering, The Ohio State University, USA

Abstract

Atmospheric rivers (ARs) are long, narrow regions of water vapor in the Earth's atmosphere that transport heat and moisture from the tropics to the mid-latitudes. ARs are often associated with extreme weather events in North America and contribute significantly to water supply and flood risk. However, characterizing ARs has been a major challenge due to the lack of a universal definition and their structural variations. Existing AR detection tools (ARDTs) produce distinct AR boundaries for the same event, making the risk assessment of ARs a difficult task. Understanding these uncertainties is crucial to improving the predictability of AR impacts, including their landfall areas and associated precipitation, which could cause catastrophic flooding and landslides over the coastal regions. In this work, we develop an uncertainty visualization framework that captures boundary and interior uncertainties, i.e., structural variations, of an ensemble of ARs that arise from a set of ARDTs. We first provide a statistical overview of the AR boundaries using the contour boxplots of Whitaker et al. that highlight the structural variations of AR boundaries based on their nesting relationships. We then introduce the topological skeletons of ARs based on Morse complexes that characterize the interior variation of an ensemble of ARs. We propose an uncertainty visualization of these topological skeletons, inspired by MetroSets of Jacobson et al. that emphasizes the agreements and disagreements across the ensemble members. Through case studies and expert feedback, we demonstrate that the two approaches complement each other, and together they could facilitate an effective comparative analysis process and provide a more confident outlook on an AR's shape, area, and onshore impact.

CCS Concepts

• Human-centered computing → Scientific visualization; Visualization application domains;

1. Introduction

Atmospheric rivers are long, narrow bands of highly concentrated water vapor in the atmosphere. They transport large amounts of moisture over great distances in a "river"-like structure, often from the tropics to the mid-latitudes [RDC*18]. ARs play a pivotal role in the Earth's hydrologic cycle and are potentially responsible for 90% of the global moisture transport [ZN98]. Regionally, they can contribute to the replenishment of freshwater and offer relief to drought conditions [DRD*11, Det13]. Locally, however, ARs have been responsible for extreme weather events by producing heavy precipitation and severely impacting human and environmental systems. Especially along the U.S. west coast, where ARs make landfall and interact with mountain environments to produce orographic precipitation [NRW*08], ultimately contributing to catastrophic flooding and landslides [HSSL00, KWN*13, RSR14]. Significant research efforts have been dedicated to understanding ARs, including analyzing their frequencies and duration [KC22], tracking their trajectories and point of landfall [GW19], exploring their relation-

ships with lower level winds [WG17] and the jet stream [SK16], evaluating their influence on snowpack [CLWR19], and identifying long-term climate trends [PDL*20].

On the other hand, there have been substantial debates on the definition and detection of ARs over the past few decades [RDC*18]. A number of AR detection methods have been established on several large datasets for different purposes, using various AR definitions. One common reanalysis quantity used in characterizing ARs is the Integrated Vapor Transport (IVT) field calculated from a combination of water vapor and wind [ZN98]. Most recent AR detection tools (ARDTs) leverage IVT for identifying ARs [GW15, ORL*20, RSR14, RKLS20]. However, these tools identify ARs with uncertainties — in particular, large structural variations — as they incorporate different geometric and temporal criteria, and use absolute or relative IVT thresholds [RSL*19]. Understanding, quantifying, and potentially reducing these uncertainties is crucial to estimate the global reach and impacts of ARs.

The Atmospheric River Tracking Intercomparison Project (ART-MIP) [RSL*19] was established to "understand and quantify uncertainties in atmospheric river science based on choice of detection/tracking methodology". The ARTMIP categorizes five main parameters used to identify and track ARs in existing ARDTs: computation type, geometry requirements, threshold requirements, temporal requirements, and regions. All participating ARDTs provide their respective AR catalogs, computed using the same underlying IVT from the MERRA-2 reanalysis dataset [GMS*17]. These catalogs describe AR characteristics such as AR regions, widths, and lengths. Since all catalogs are produced from the same dataset, ARTMIP enables a fair comparison among all participants.

With the growing interest in ARs, few existing research have considered uncertainty visualization of an AR ensemble. A common uncertainty visualization of ARs overlays their boundaries onto a background map (e.g., [LSR20, RSL*19]). As the number of ARDTs grows, visual clutter becomes a major challenge affecting the effectiveness of the visualization. By leveraging existing ARTMIP catalogs, we quantify and visualize the uncertainties associated with an ensemble of ARs identified by a set of ARDTs. Specifically, we focus on visualizing the boundary and interior uncertainties that reflect structural variations of an ensemble of ARs. Our contributions include:

- We provide a statistical overview of the AR boundaries using contour boxplots [WMK13] that highlight the structural variations of AR boundaries based on their nesting relationships.
- We introduce the topological skeletons of ARs based on Morse complexes, referred to as AR skeletons, that characterize the variations among the IVT fields interior to an ensemble of ARs.
- Additionally, we define and extract topological axes from AR skeletons that reflect the structure of the underlying IVT fields by tracing the direction of maximum IVT strengths.
- We propose an uncertainty visualization of topological skeletons, inspired by MetroSets [JWKN21], that highlights the agreements and disagreements among the topological skeletons across the ensemble members. This visualization is achieved by a novel straightening step that helps to better align the skeletons.
- We demonstrate via multiple case studies and expert feedback that our uncertainty visualizations are effective in estimating impacts and producing useful insights of ARs.

2. Related Work

Uncertainty quantification is crucial for climate applications, especially for studying extreme events. With increasing computing resources, ensemble datasets are created to express the uncertainties generated by a collection of methods. Such information could be useful in guiding infrastructure design, planning, and maintenance. In this section, we first review related work on ensemble and uncertainty visualization with a focus on climate applications. We then discuss the characterization and uncertainty visualization of ARs.

Ensemble and uncertainty visualization. Wang et al. [WHLS19] categorized ensemble visualization based on ensemble data types, visualization techniques (point, curves, surfaces, volumes, and non-spatial representations), and analysis tasks (overview, compare, cluster, trends, features, and parameters). Ensemble data introduce uncertainty due to multiple instances of the same physical quantity [WHLS19]; see uncertainty visualization surveys [PWL*97, PRJ12, KDJ*21] with [Pan08] focusing on natural hazards.

In meteorology and climatology, uncertainty visualization is often used to analyze ensembles of simulation data. Potter et al. [PWB*09] presented Ensemble-Vis, an interactive tool that provides a set of overview and statistical displays that highlight the probabilistic characteristics of ensemble data. They focused on applications in short-term weather forecasting and climate modeling. Biswas et al. [BLLS17] explored the uncertainty in time-varying weather simulation ensembles. They investigated the sensitivities of input parameters and compared accuracies across varying resolutions. Sanyal et al. [SZD*10] introduced a tool called Noodles that visualizes point and curve-based uncertainties, with applications in numerical weather prediction ensembles. They used graduated uncertainty glyphs and ribbons to show the uncertainty of ensemble members and the ensemble as a whole, respectively. For curve-based uncertainties, Zhang et al. [ZCL*21] proposed a novel method of variable spatial spreading and generated spaghetti plots to show the uncertainty of each variable. Their interactive tool was used to identify important features within a weather forecast ensemble and to investigate the global and local consistencies. Whitaker et al. [WMK13] introduced contour boxplots that compute order statistics on an ensemble of contours based on their nesting relationships. They extended contour boxplots to streamlines and pathlines and introduced curve boxplots [MWK14]. Both techniques were used in visualizing an ensemble of hurricane tracks and weather forecast simulations.

Several recent techniques focus on structural variations among topological descriptors. Yan et al. [YWM*20] studied structural averages of an ensemble of merge trees. Athawale et al. [AMY*22] visualized the uncertainty of an ensemble of 2D Morse complexes. They derived statistical summaries for the Morse complexes and demonstrated the effectiveness of their visualization via scientific datasets, including wind forecasting and ocean eddy simulation. In this paper, we also propose an uncertainty visualization of Morse complexes. Whereas Athawale et al. introduced statistical summary maps that characterize the uncertain behavior of gradient flows, our work focuses on the structural variations of AR skeletons, which are 1D skeletons of Morse complexes of the IVT field interior to the ARs. In our setting, each AR skeleton is a subset of the Morse complex computed from the same underlying IVT field.

Characterization and uncertainty visualization of ARs. Characterizing ARs has often been a challenging task due to their varying geometric and temporal features. Rutz et al. [RSL*19] characterized AR events by their frequency, duration, seasonality, and other metrics related to water vapor transport. Inda-Diaz et al. [IDOZC21] studied the sizes of ARs, including their lengths, widths, and areas. Wick et al. [WNR13] characterized ARs using the positions of their axes. To estimate an AR axis, they used skeletonization, an image processing technique that reduces an AR region to a spine with single-pixel width that is equidistant to the boundaries. Guan and Waliser [GW15, GW19] introduced an axis extraction method that aimed to capture the maximum IVT strength along the direction of the AR. We propose a topology-based method to compute a topological skeleton based on

a gradient-based topological descriptor called the Morse complex, which captures the IVT structure inside an AR region. A topological axis could then be extracted from the topological skeleton.

Since the initiation of ARTMIP, much research has emerged to understand the uncertainties of an AR ensemble formed from a set of ARDTs. As an early ARTMIP study, Ralph et al. [RWS*18] conducted a performance analysis of ARDTs at a specific location in California. They measured the sensitivity of the frequency, duration, and intensity of ARs to a chosen ARDT. They concluded that the ARDTs with more restrictive geometric requirements and higher IVT thresholds identified fewer AR events. Chen et al. [CLG*18] investigated the relationship between ARs in the western U.S. and precipitation, whereas Shields et al. [SWMC*22] focused on evaluating uncertainties of Antarctic ARs. Zhou et al. [ZOU*21] studied the uncertainties in the AR lifecycles based on the ARDT and found an increase in agreement of landfall activities for stronger AR events. Rutz et al. [RSL*19] analyzed over 20 AR detection and tracking methods to quantify uncertainties (in AR frequency, duration, and intensity) on a climatological global scale from 1980 to 2017. Lora et al. [LSR20] also investigated AR consensus on a global scale. They found that most discrepancies occurred during small and weak events, but ARDTs mostly agree on general AR footprints.

Regarding visualization techniques, traditional boxplots, scatterplots, histograms, and line charts are often used to describe statistical summaries of the AR characteristics [ZOU*21, RSL*19, ORL*20]. Rutz et al. [RSL*19] used panel charts (multiple charts arranged in a grid) of focused AR regions to compare ARDTs. Lora et al. [LSR20] also used panel charts to show the spatial distributions of AR frequencies. In addition to overlaying AR boundaries [RSL*19, LSR20], we apply contour boxplots [WMK13] to study their structural variations.

3. Background

Morse complexes. Let $f : \mathbb{M} \subset \mathbb{R}^2 \to \mathbb{R}$ be a continuous function defined on a 2D smooth manifold. A point $x \in \mathbb{M}$ is a *critical point* if its gradient $\nabla f(x) = 0$; otherwise it is a *regular point*. f is a *Morse function* if all critical points of f are nondegenerate. Given a Morse function f, an *integral line* is a maximal path at any regular point x whose tangent vectors agree with the gradient [EHZ01]. Each integral line starts and ends at a critical point, i.e., a maximum, minimum, or saddle point. The *descending manifold* surrounding a local maximum p includes p itself and all regular points whose integral lines end at p. The descending manifolds decompose the domain into 2-cells, whereas integral lines connecting the critical points are the 1-cells, and critical points are the 0-cells. These cells form a complex called a *Morse complex* of f. For example, given a 2D Morse function in Fig. 1 (A), the descending manifold of the local maximum p in Fig. 1 (B) is colored in green. Points inside the green 2-cell have integral lines ending at p.

In our setting, we compute the 1D skeleton of the Morse complex of an IVT field f defined on a 2D domain, which is formed by the local maxima and saddles connected by 1-cells. The 1D skeleton inside an AR region is its topological skeleton (AR skeleton, in short). We apply persistence simplification [ELZ00] to Morse complexes to remove noise and retain significant features.
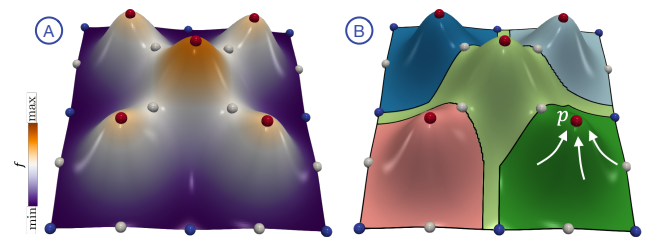

Figure 1: *(A) A graph $(x, f(x))$ of a Morse function f. (B) Descending manifolds forming the Morse complex of f: colored regions are 2-cells; black lines are 1-cells; red, blue, and gray points denote local maxima, local minima, and saddles, respectively.*

Contour boxplots. Whitaker et al. [WMK13] introduced contour boxplots as a generalization of the conventional boxplots. Contour boxplots extend the notion of *band depth* [LPR09] to quantify the nesting relations among a set of contours. Given an ensemble of sets, the *set band depth* of a set for a given j is the probability that the set lies in the *band* defined by a random selection of j sets from the ensemble. Formally, given an ensemble of sets $E = \{S_1, \ldots, S_n\}$, where $S_i \subset U$ with U being the universal set. A set $S \in E$ is considered to be an element of a *band* of j other sets $(S_1, \ldots, S_j \in E)$, denoted as $sB(S_1, \ldots, S_j)$, if it is bounded by their intersection and union [WMK13],

$$S \in sB(S_1, \ldots, S_j) \iff \cap_{k=1}^{j} S_k \subset S \subset \cup_{k=1}^{j} S_k.$$

Then the set band depth (sBD) is defined as

$$sBD_J(S) = \sum_{j=2}^{J} P[S \in sB(S_1, \ldots, S_j)].$$

Applying sBD to contours, Whitaker et al. introduced the *contour band depth* (cBD) and provided an algorithm for its computation. They additionally relaxed the definition of subset and introduced a parameter ε to allow a small percent of each set to violate the traditional definition of subset.

We model an ensemble of AR boundaries as contours and apply contour boxplots to provide an overview of their distribution. We compute the cBD for each AR boundary. A ranking of cBD from maximum to minimum produces a median-to-extrema ordering of the AR boundaries. Similar to box plots, the boundary with the largest cBD corresponds to the median, and the middle 50th percentile includes the boundaries in the first half of this ranking.

MetroSets. Jacobsen et al. [JWKN21] introduced MetroSets for visualizing set systems. An input set system is modeled as a hypergraph $H = (V, E)$ where V is the set of vertices and E is the set of hyperedges. Using the metro map metaphor, each vertex in V represents a metro station, and each hyperedge in E represents a metro line. The MetroSets visualization imposes the constraint that the edges are only allowed to be horizontal, vertical, or have an angle of $\pm 45°$. Given these constraints, the system optimizes for several desirable properties such as minimum edge crossings, monotone metro lines, and uniform distances between adjacent stations. We introduce an uncertainty visualization of AR skeletons, inspired by MetroSets, that highlights their structural variations.

4. Data

All participating ARDTs of ARTMIP identify AR regions with the same IVT fields from MERRA-2 reanalysis data [GMS*17] (provided by the NASA Global Modeling and Assimilation Office) [RSL*19]. MERRA-2 IVT is a 3-hourly dataset with a horizontal resolution of $0.625° \times 0.5°$. The IVT is calculated as

$$IVT(kg \cdot m^{-1} \cdot s^{-1}) = \frac{1}{g} \int_{P_{sfc}}^{P_{top}} qV dp,$$

where g is the gravitational acceleration, q is the specific humidity, and V is the horizontal vector wind. MERRA-2 IVT is calculated from 1000 hPa (P_{sfc}) to 300 hPa (P_{top}) using 21 pressure levels [CDMCR21]. IVT has the unit $kgm^{-1}s^{-1}$ to indicate the amount of water vapor transported over a single grid per second.

We use a subset of 13 representative ARDTs from ART-MIP suggested by AR experts and prior works: `ar_connect`, `climatenet`, `guan_waliser_v3`, `mundhenk_v3`, `panlu`, `reid500`, `rutz`, `sail_v1`, `teca_bard_v1.0.1`, `tempest_250`, `tempest_500`, `tempest_700`, and `lora_v2`. For each ARDT, we use 6-hourly catalog data that include the AR regions identified at each time step. For `guan_waliser_v3`, AR axes are also provided. Our analysis focuses on individual AR case studies (on January 7–9, 2017 and October 23–24, 2006) supplemented with some statistics for the years 2017 and 2006.

5. Method

Given an ensemble of ARs produced by 13 ARDTs of the ART-MIP catalogs, we examine uncertainties that arise from boundary (Sec. 5.1) and interior variations (Sec. 5.2) of ARs. We also discuss our method for extracting the topological axes of ARs (Sec. 5.3).

5.1. Boundary Variations

Given an ensemble of ARs, we first overlay AR boundaries on top of a shared IVT field, see Fig. 2 (left) for an example. Each boundary is colored by its corresponding ARDT using a categorical colormap. The IVT field in the background is visualized using a diverging colormap together with a world map in orange.

From a complementary viewpoint, we compute a contour boxplot with $\varepsilon = 0.001$, allowing tolerance in computing contour band depth (cBD) when the AR boundaries intersect. We obtain a ranking of the ARDTs from the maximum to the minimum cBD: `lora_v2`, `ar_connect`, `teca_bard_v1.0.1`, `panlu`, `mundhenk_v3`, `rutz`, `tempest_250`, `tempest_500`, `reid500`, `tempest_700`, `sail_v1`, `guan_waliser_v3`, and `climatenet`. This ranking orders the AR boundaries by size. The interquartile range (IQR), i.e., middle 50th percentile, is composed of the first six ARDTs in the ranking that identify ARs that are medium in size, the 75th percentile contains the first nine. We show this hierarchy in the contour box plot with a sequential colormap where black represents the IQR, purple the 75th percentile, and orange the 100th percentile. In the example in Fig. 2 (right), the IQR is drawn in a thin black band, indicating high agreement among the ARDTs in the middle 50th percentile. The ARDTs between the 50th and the 75th percentile all identified

slightly smaller regions for this AR. We confirm this observation in the overlaying boundary plot (left) where `tempest_250`, `tempest_500`, `reid500` produce smaller AR boundaries. For the ARDTs between the 75th and the 100th percentile (drawn in orange), we have the smallest (`tempest_700`) and the largest AR boundaries (`sail_v1`, `guan_waliser_v3` and `climatenet`, respectively).
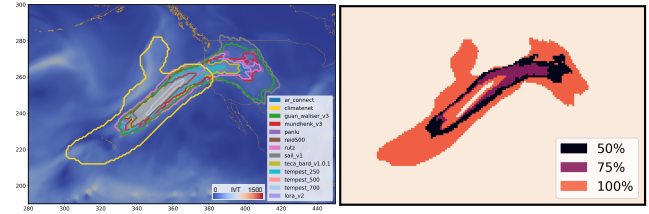

Figure 2: *Boundary variations of an AR ensemble identified on February 15, 2014. Left: an overlaying boundary plot. Right: a contour boxplot.*

Although the overlaying boundary plot may be sufficient to show the distribution of a few AR boundaries, as the sample size (i.e., number of ARDTs) increases, visual occlusion and clutter become major challenges for readability and interpretation. The benefit of a contour boxplot is that it provides a scalable and clear statistical view of an ensemble of AR boundaries. In this example, we observe high agreement among the ARDTs in the IQR, and an increase in boundary variations between the 50th and 75th percentile drawn in purple, indicating an increase in uncertainty. The orange region between the 75th and 100th percentile shows the highest disagreement between ARDTs in this band and others in the ensemble.

5.2. Interior Variations

To the best of our knowledge, existing methods that investigate the uncertainty of an ensemble of ARs focus exclusively on the variations in the AR boundaries. We propose to investigate, in addition to the boundary variations, the interior agreements and disagreements of an AR ensemble. Our framework consists of three steps:

1. *Characterization.* We first summarize the interior structure of an AR region by computing the Morse complex of its underlying IVT field and extracting its 1D skeleton. The resulting topological skeleton captures the maximum strengths of the underlying IVT field interior to the AR region.
2. *Straightening.* We further simplify the topological skeleton of an AR to a graph with straight edges between selected nodes. We create a metro map representation for each AR.
3. *Uncertainty Visualization.* Given an ensemble of ARs in the same region at the same time step, identified by an ensemble of ARDTs, we compute a metro map for each member. We construct the MetroSets visualization by overlaying the individual metro maps and shifting them strategically to reveal all edges.

5.2.1. Extracting Topological Skeletons

Inspired by previous works [WNR13, GW19] that characterized an AR using an *AR axis*, we propose a topology-based method that characterizes the interior structure of an AR with a graph, referred to as its *topological skeleton*. For each AR, our framework takes two inputs: the AR region given by the catalog data of an ARDT,

and the underlying IVT field from the MERRA-2 dataset. The output is the 1D skeleton of the Morse complex of the IVT field interior to the AR region, referred to as the topological skeleton. The Morse complex traces the maximum-saddle connections of the IVT field, reflecting the underlying trend of the maximum IVT direction.

In order to separate noise from the significant features in the IVT field and the subsequent Morse complex, we first apply persistence simplification to the IVT field. The level of simplification depends on a predetermined simplification threshold. The resulting Morse complex preserves the significant topological structures that correspond to prominent IVT trends. We then extract the 1D skeleton of the Morse complex interior to the AR region.

The AR regions given by the catalog data are binary indicator matrices with 1 representing the inside of the AR region and 0 outside. We treat the pixels with a value 1 as a point cloud. We first define the AR boundary using an alpha shape [EKS83], which in 2D is a set of piecewise linear curves associated with the shape of the point cloud (generalizing the notion of a convex hull). We set the alpha shape parameter $\alpha = 1$ as the data lie on a grid with a 1-pixel resolution. The 1D skeleton of the Morse complex is computed using TTK [TFL*17] and intersects the alpha shape. We identify intersection points and extract the subset of the 1D skeleton inside of the AR region, resulting in the topological skeleton.

Occasionally, the initial topological skeleton may leave the catalog AR region for a short distance before traversing back into the region, leading to a disconnected skeleton. The phenomenon occurs mostly in two scenarios, as shown in Fig. 3 (B), when the original AR region has a narrow section, or as an artifact of the TTK Morse complex computation. To ensure the connectedness (continuity) of the skeleton, we introduce a tolerance parameter r, which represents the radius (in pixels) that we allow the skeleton to be outside the AR region. We set $r = 2$, as it is the smallest tolerance in our experiments to ensure connectedness of the topological skeletons. Fig. 3 (A) shows an AR with the catalog region drawn in white dots in the background and the topological skeleton in yellow. We zoom into the region in the box in (B) and (C). When $r = 0$, the skeleton is disconnected due to the irregularities in the AR geometry (B). It becomes connected when $r = 2$ in Fig. 3 (C). A connected skeleton supports the extraction of a topological axis (see Sec. 5.3), an example of which is shown in red in Fig. 3 (A).

5.2.2. Straightening Topological Skeletons

Given an ensemble of ARDTs that produce different AR regions (in the same area at a given time step), we aim to examine their interior variations. Since these AR regions share the same underlying IVT field, their associated topological skeletons overlap in shared regions. To visualize multiple skeletons simultaneously, we adapt the MetroSets visualization for a set system. In the original MetroSets [JWKN21], vertices are metro stations and edges are stacked to show the sections of routes shared by multiple metro lines. Since Morse complexes are computed from a triangulated domain, their 1D skeletons have complicated geometry, making the stacked edges difficult to interpret. We propose a straightening strategy that further simplifies a topological skeleton before stacking them. We call a straightened AR skeleton the *metro map* of an AR.

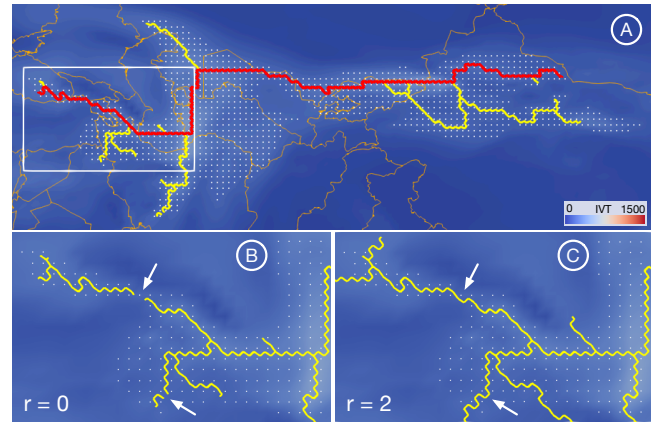We aim to straighten the edges of the skeleton while preserving

Figure 3: *(A): the topological skeleton (yellow) and topological axis (red) of an AR region identified by* guan_waliser_v3 *shown in white dots. (B) and (C) are zoomed-in views of the region in the box, where $r = 2$ reconnects the skeleton.*

its topological structure. We first identify the boundary nodes (degree 1) and intersection nodes (degree larger than 2) and use them as the metro map stations. Consecutive edges connected by degree 2 nodes are deemed redundant because they do not contribute to any topological change in the skeleton. Therefore, we combine consecutive degree 2 nodes into a single edge. Fig. 4 (D) illustrates this process where the green and orange nodes are the boundary and intersection stations, respectively. We connect these stations with straight edges using nearest-neighbor searches that respect the topology of the skeleton. Starting from an intersection station, we traverse the skeleton in each branch direction until we reach and connect with the closest neighboring station on each branch. Assuming that there are no isolated stations in the topological skeleton, we complete the construction of the metro map when we finish the nearest neighbor search for all intersection stations. Fig. 4 (E) displays the original AR identified by guan_waliser_v3 and its topological skeleton in blue and the straightened skeleton in red. The final metro map of the AR is displayed in (F).
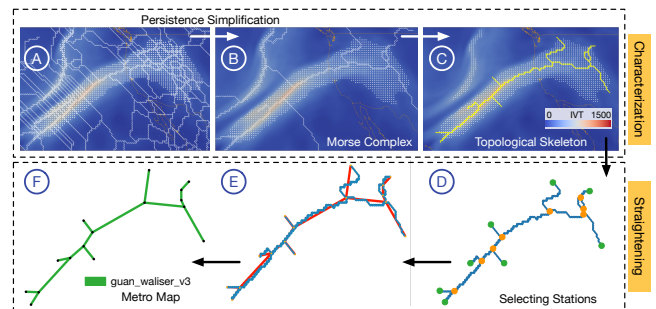

Figure 4: Characterization *and* Straightening *pipeline.*

5.2.3. Uncertainty Visualization of Skeleton Ensembles

Given an ensemble of ARs, we compute metro maps (i.e., straightened topological skeletons) that capture their interior structures. To capture the interior variations, we introduce an uncertainty visualization of the skeletons by overlaying metro maps using MetroSets.

We first need to deal with a minor technicality. If we simply

overlay multiple metro maps, the boundary edges connecting with the boundary stations may be misaligned across multiple skeletons. This issue occurs when the boundary edges originating from the same intersection node v (of multiple skeletons) terminate at different boundary stations; see Fig. 5 (A) for an illustration where the green and orange regions belong to two different ARs, respectively. Ideally, the boundary edges that belong to the same section of a topological skeleton should overlap, i.e., edges with the same label (i.e., label 1 and label 2) in Fig. 5 (B) should share the same direction. Therefore, we correct the directions of these boundary edges that originate from station v. To do so, we compute pairwise angles between these boundary edges and group the edges based on the proximity of these angles. The boundary edges in Fig. 5 (B) are split into groups 1 and 2. We use the longest edge in each group as the final directions of the stacked edges in the metro map. We apply an orthogonal projection to correct the directions of all other shorter edges in each group, see Fig. 5 (C).
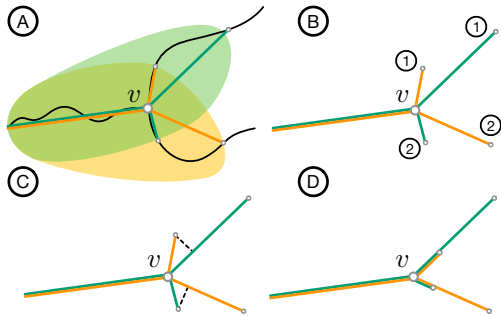

Figure 5: *Realigning boundary edges from multiple metro maps.*

Now we have multiple metro maps superimposed upon each other. The last step of our pipeline is to shift the edges strategically to avoid visual occlusion. The original MetroSets visualization [JWKN21] imposed the *octolinearity* constraint on each edge to simplify the shifting process. Octolinearity restricts all edges to have slopes of a multiple of $45°$, which provides significant convenience when shifting edges. However, MetroSets is designed for tabular data for which geometric locations need not be considered. Our case differs as the stations originate from the topological skeletons of the ARs, and we are required to preserve their geometric locations. We name the stacked edges in the MetroSets *super-edges*. From the ensemble, we are given an arbitrary order of ARDTs, which corresponds to the order of the edges in the super-edges of the MetroSets. We maintain the same order for the subset of ARDTs present in each super-edge during edge shifting, except that we reverse the order when the edges have negative slopes to ensure continuity in the MetroSets. The shifting directions are orthogonal to the edge directions. In Fig. 5 (D), super-edges with positive, and negative slopes are composed of edges with opposite orders.

In Fig. 6, we show our MetroSets visualization for an AR detected on November 1, 2006, at 12 am. On the left, we have examples of individual metro maps and AR boundaries from four different ARDTs. The metro maps are drawn in different colors that correspond to the edge colors in the MetroSet. Some super-edges in the MetroSet encode all ARDTs that detected an AR in the same region. We use a thick orange edge to represent these sections of the AR skeletons that show complete agreement among the ARDTs.
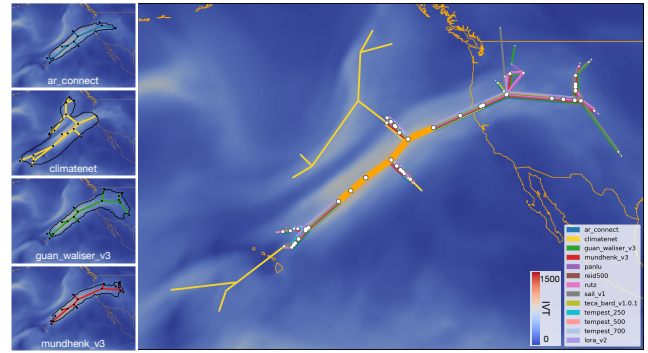

Figure 6: *MetroSets visualization for the interior variations of an AR identified on February 15, 2014. Left: the metro maps for four individual ARDTs and their identified AR boundaries drawn in black. Right, the MetroSet for an ensemble of all 13 ARDTs.*

5.3. Topological Axes

Furthermore, we could define and extract topological axes from AR skeletons. Since most ARs in the catalog have elongated shapes, the axes of an AR should intuitively follow the direction of the *diameter* of an AR region (i.e., the largest distance that can be formed between two opposite parallel lines tangent to its boundary). Given a topological skeleton of an AR, we first select nodes in the skeleton that are furthest apart from each other and then define their shortest path in the skeleton to be its topological axis. Fig. 3 (A) shows an example AR with its topological axis drawn in red. Together with (B) and (C), Fig. 3 illustrates the importance of having a connected skeleton to compute a topological axis. Compared to the axis extraction method by Guan and Waliser [GW19], we extract the axis from our topological skeleton. We remove noise and less important features from the underlying IVT field using persistence simplification; see Fig. 4 (A)-(B). Thus, we are less likely to be stuck in local maxima or deviate from the main direction of the AR. Compared to the AR axis extracted by an image-based skeletonization method [WNR13] that considers only the AR geometry, our topological axis reflects the structure of the underlying IVT field by tracing the direction of maximum IVT strengths.

6. Case Studies

We apply our uncertainty visualization techniques to study boundary and interior variations of AR ensembles. We focus on two representative AR events as case studies: a strong AR event on January 7–9, 2017, and a weak AR event on October 23, 2006. We use 6-hourly data for both events. Martin Ralph et al. [RRC*19] introduced a scale for the intensity and impact of ARs, mainly considering two parameters: maximum IVT within the AR region and the duration of AR conditions. The scale separated ARs into categories 1–5, from weak to strong. According to this scale, our 2017 event is a Category 4 AR event, which is described to be "mostly hazardous, but also beneficial." On the contrary, our 2006 case study is a Category 1 AR event that is "primarily beneficial."

Overview of results. We demonstrate that the three types of uncertainty visualizations—boundary plots, contour boxplots, and MetroSets—produce different insights for AR analyses. We emphasize the advantage of contour boxplots and MetroSets over the

original boundary plots by examining the boundary and interior variations of the ensemble using these visualizations and the scientific insights they produce. Whereas a boundary plot displays a geometric overview of the individual AR boundaries, a contour boxplot visualizes a statistical overview of the boundary distributions, thus highlighting boundary variations among the regions of AR ensembles. Using contour boxplot derived statistics, we could investigate agreement and disagreement among the AR catalogs produced by the 13 ARDTs. In particular, we observe their respective differences in thresholding and geometric requirements as components of their AR detection criteria in relation to the distribution. By inspecting the contour boxplots over time, we can identify temporal changes in the AR from an ensemble perspective.

On the other hand, MetroSets-inspired visualization highlights the interior variations of an AR ensemble. The (straightened) topological skeletons used in the MetroSets provide a structural summary of the ensemble. Compared to the original boundary plots, the MetroSets show clear interior structural similarities and differences among the ARs extracted by different ARDTs.

Furthermore, we observe a strong correlation between high-intensity AR events and high agreement among the AR topological skeletons extracted by different ARDTs, indicating that most ARDTs can capture strong ARs, but not moderate and relatively weaker ARs which can still impact certain regions. Additionally, using (known) precipitation anomalies which directly indicate ARs' impact, we show that the MetroSets facilitates the prediction of AR landfall locations and potential AR impact regions (after the AR makes landfall and dissipates).

Finally, we compute topological axes of ARs and compare them against existing method by Guan and Waliser [GW19]. We show that our topological axes span the entire AR regions and are more consistent across consecutive time steps.

6.1. Case Study: Strong AR Event in 2017

California experienced a series of strong AR events in January and February 2017. Although these AR events alleviated the state's water storage deficit, they caused disastrous flooding and landslides in the Bay Area, and significantly damaged the Oroville Dam's spillways [WBCL18]. In this case study, we examine the AR ensemble from an AR event on January 7-9, 2017. During this three-day period, an observation site in Venado (California) recorded more than a foot of precipitation. Sacramento (California) witnessed its fourth-highest January rainfall on record, almost doubling the January average rainfall. Higher elevation mountain ranges, such as the Sierra Nevada Mountains, experienced record-breaking snow falls [DL17].

The contour boxplots enable us to compute a statistical distribution for an ensemble of AR boundaries. Fig. 7 shows the ARDT identification frequencies computed from the contour boxplots. The green line reflects the total number of ARs identified by the ARDTs during this event. The stacked blue and orange bars show the frequencies each ARDT appear in the 50th and the 75th percentile, respectively. The AR event from January 2017 is shown on the left. Over the 12 ARDTs in the ensemble, at least 10 identified an AR in the region at 8 of the 12 time steps, which indicates high agreement
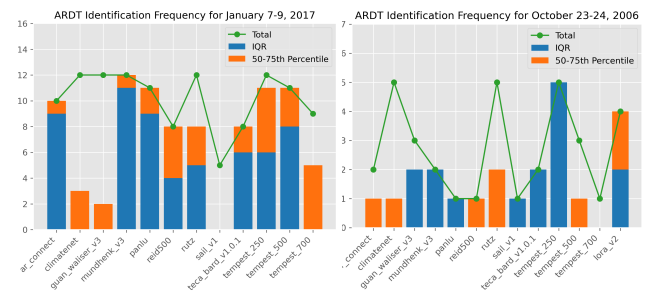

Figure 7: *ARDT identification frequencies based on the contour boxplots. Left: an AR event from January 7-9, 2017. Right: an AR event from October 23-24, 2017.*

on the existence of this AR event, correlating with the high intensity of the event. We analyze the types of ARDTs in each percentile. For this event, the top three ARDTs that consistently appear in the IQR (middle 50th percentile) are `ar_connect`, `mundhenk_v3` and `panlu`. Both `mundhenk_v3` and `panlu` use relative IVT thresholds with geometric constraints as their main identification criteria, whereas `ar_connect` uses a region growing methodology with static IVT thresholds for the core and the boundary of the AR. In contrast, the top three ARDTs that appear in the 50th-75th percentile band are `tempest_250`, `tempest_700` and `reid500`, all of which use absolute IVT thresholds.
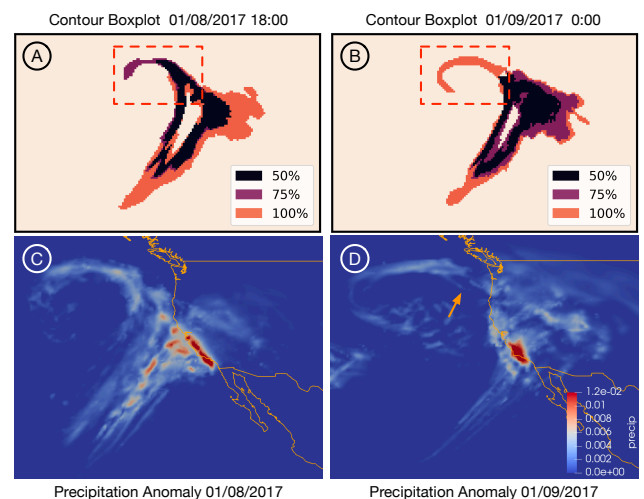

Figure 8: *A and B are contour boxplots from two consecutive time steps that show the changes in the ARDTs' representations of the AR's low pressure system. C and D are the precipitation anomalies of the corresponding days that reflect the impact of the AR.*

The contour boxplots over consecutive time steps also highlight the temporal changes of the AR ensemble, in terms of the agreement and disagreement of AR regions across ensemble members. In Fig. 8 (A) and (B), we show the contour boxplots of January 8 at 6 p.m. and January 9 at midnight. The regions in black, indicating the AR boundaries from the IQR, remain relatively narrow and mostly consistent. This shows high agreement among the ARDTs regarding the boundary of this AR. The regions in the red boxes signify the only significant change across the two time steps, indicating the northwest to north central region to be an area of interest.

To examine the impact of the AR, we inspect the corresponding daily precipitation anomaly plots shown in Fig. 8 (C) and (D). A daily precipitation anomaly is computed using the daily precipitation during the AR event subtracting the daily average precipitation of the month of January over a period of 42 years (from 1980 to 2021). As the AR forms, moisture moves up ahead of the cold front that forms the main body of the AR. As time progresses, the moisture gets wrapped into a low pressure system that forms the curve at the northwest section of the AR. At 6 p.m. on January 8, 2017, there is high agreement among the ARDTs for the low pressure system of the AR. Six hours later, the same section of the AR exhibits a low degree of agreement among the ARDTs. This effect is reflected in the precipitation anomaly of the corresponding regions. In Fig. 8 (C), there is higher precipitation in the region of the low pressure system. In Fig. 8 (D), there is lower precipitation in the same region and a gap appears in the precipitation distribution indicated by the orange arrow. This gap corresponds to the boundary of the AR region for many ARDTs.

However, the moisture in the low pressure system continues to impact the corresponding area on the ocean, and we can appreciate ARDTs that account for this moisture. From the MetroSets visualization of the same time step in Fig. 9, we know that `rutz` and `sail_v1` are the two ARDTs that continue to characterize this low pressure system towards the end of the AR event.

We continue to study the AR event using the MetroSets visualization; see Fig. 9. Throughout this case study, the MetroSets are computed using an absolute persistence threshold of 30, selected by balancing the degree of clarity and the level of details in the MetroSets. We overlay MetroSets with the underlying IVT fields, where all IVT fields across all time steps have consistent scaling. In the MetroSets visualization, the legends with empty boxes indicate that the corresponding ARDT algorithms did not identify an AR in this region (at the particular time step). The thick orange edges in the MetroSets represent complete agreement among all ARDTs that identified an AR in the region (at the particular time step).

The MetroSets visualization gives us a more detailed overview on the interior variations of the individual ARs produced by different ARDTs. For this high-intensity event, almost all ARDTs agree on the existence of the AR across most time steps. Looking at the underlying IVT field, the AR is of the highest intensity between 6 a.m. on January 8 and midnight of January 9. Following the thick orange edge of the core section of the AR during this period in Fig. 9, we see that there is high agreement among ensemble members that the AR moved toward the direction of Sacramento (as indicated by the yellow star).

At 12 p.m. on January 8, 2017 (see Fig. 9), the AR impact splits into two directions, one to the north toward the ocean and the other around and to the south of Sacramento. The core section of the AR, identified by all but 2 ARDTs in the ensemble, continued to move toward the Sacramento direction at 6 p.m. on January 8. The second direction of the split in the MetroSets sustained the highest impact from the AR on land. The two figures on the right of Fig. 9 show the precipitation anomaly of January 8 and 9, 2017. Apart from the high impact on the costal region, Sacramento is located exactly in the inland region of high precipitation anomaly. Moreover, as time

progresses, the MetroSets visualizations clearly show that the AR impact moves more inland and south during the next 12 hours.

This insight is further confirmed by the precipitation anomaly plot on January 9, 2019, where the precipitation spreads into more inland regions. An additional observation from the MetroSets is that the ARDT `guan_waliser_v3` (drawn in green) consistently captures the moisture with further land penetration, indicated by the red boxes in the MetroSets. The corresponding red box in the precipitation anomaly plot shows that although many ARDTs do not consider these inland moisture as part of the AR, they still cause a significant impact on the precipitation of the region as time progresses. This information could be useful for scientists studying inland AR activities in states such as Utah and Colorado.
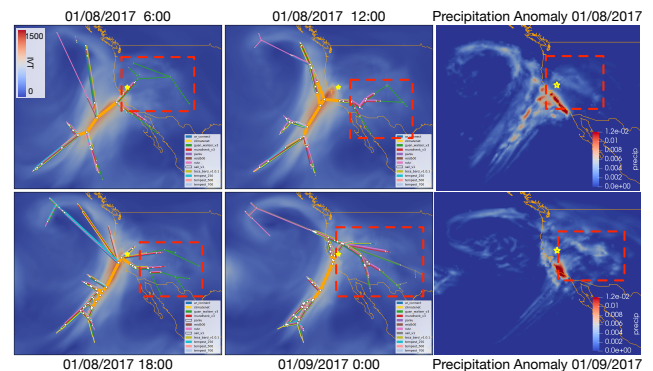

Figure 9: *We show how MetroSets inform scientists about AR impact. The yellow star marks the location of Sacramento and the red boxes show the inland penetration of* `guan_waliser_v3`. *Left: the MetroSets in 6-hour intervals on January 8, 2017. Right: precipitation anomaly for January 8 and 9, 2017.*

6.2. Case Study: Weak AR Event in October 2006

Our second case study follows an AR event from October 23 to 24, 2006, which terminates along the coast of British Columbia. The relatively weak AR event brought light precipitation with no significant impact. Rutz et al. [RSL*19] provided a brief analysis of this event and stated that the ARDTs generally disagreed with the occurrence of AR conditions during this period. Specifically, `rutz` and `tempest` methods most frequently identified the AR. We confirm their findings but provide additional insights.

Due to the low intensity of the AR event, ARDTs show minimal agreement on its existence. Statistical analysis via contour boxplot (see Fig. 7 right) reveals that `rutz`, `tempest_250`, and `climatenet` most commonly detected the AR. These methods feature less stringent IVT thresholds and geometric criteria. More restrictive methods such as `panlu`, `reid500`, and `tempest_700` only identified one AR over the five time steps. This observation confirms the findings from Rutz et al. [RSL*19] that more restrictive methods often miss weak AR events, whereas less restrictive methods detect both strong and weak events. Apart from `tempest_250`, `guan_waliser_v3`, `mundhenk_v3`, `teca_bard_v1.0.1` and `lora_v2` are also often in the IQR of the AR boundary distribution. Among all above ARDTs, `tempest_250` is the only one using absolute IVT threshold, highlighting the effectiveness of methods using relative IVT thresholds,

especially in detecting weak AR events. In Fig. 10, we show the overlaying boundary plots and contour boxplots at the start of the AR event. Most ARDTs in the ensemble identified the AR at these two time steps. The 50 percentile bands in the contour boxplots are narrow, indicating high agreement on the region of the AR.
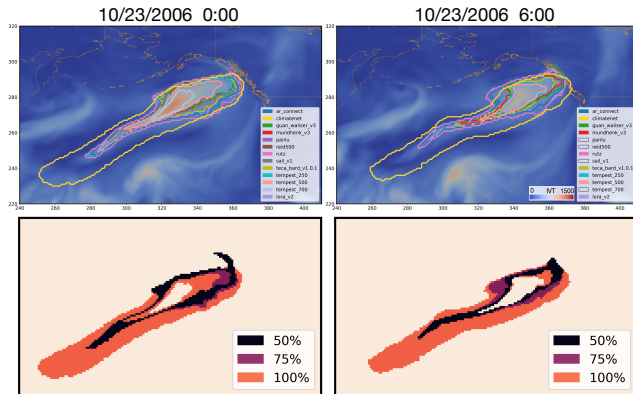

Figure 10: *The overlaying boundary plots and contour boxplots at the start of the AR event.*

We show the MetroSets visualization of this AR event in Fig. 11. On the top, we have the MetroSets at 6-hour intervals. On the bottom, we show the precipitation anomaly on October 23 and 24, 2006. Since this AR event has less complex geometric structures than the one from the previous case study, we use a reduced absolute persistence threshold of 20 to compute the MetroSets. We can deduce low intensity of the AR event by the high disagreement among the ARDTs on the existence of this AR.

Following the thick orange edge in the MetroSet visualization in Fig. 11, we see that the core section of the AR decreases in length as it moves toward the coast and also to the south as time progresses. This indicates that the ARDTs agree on the trajectory of the AR and the potential impact region. The corresponding precipitation plots depict the same pattern that the precipitation moved towards the southern part of the coast. Nevertheless, there is substantial disagreement for the section of the AR approaching land. Over time, a few ARDTs persisted in identifying an AR in the region. The remaining ARDTs at 12 p.m. and 6 p.m. show that the AR impact diverges into multiple directions, with minimal land penetration, see the red boxes in Fig. 11. This suggests that the effect of the AR dissipated as it approached land. The precipitation anomaly on October 23 and 24 reflects this transition precisely.

In Fig. 11 (A), there was high precipitation on the coast and also in the ocean. By October 24, shown in Fig. 11 (B), there was little precipitation observed on land or the ocean, although some precipitation continued to occur along the coast. The MetroSets also show that `climatenet` consistently identifies a much larger region than other algorithms, especially in the southwest direction. `climatenet` is the only ARDT that uses deep learning techniques and it produces drastically different results compared to other methods. `Rutz` also identifies a larger region for the AR for most of the time steps. For the last time step, `Rutz` connects two regions with relatively high IVT values and identifies a region much larger than any other algorithm in the ensemble. From the precipitation plot, we deduce that `rutz` is potentially connecting multiple AR regions.
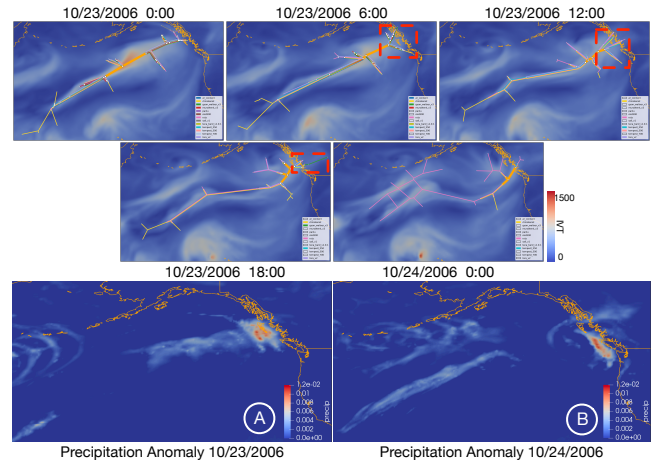

Figure 11: *Top: AR event progressions in 6-hour intervals on October 23. Bottom: precipitation anomaly on October 23 and 24, 2006.*

6.3. Case Study: Topological Axes of AR

In this case study, we compare our topological axes and the AR axes computed from `guan_waliser_v3`. `Guan_waliser_v3` uses a local search method that first identifies the pixel with the maximum IVT value and traces the axis along the overall IVT direction. We use the topological skeleton of the AR which we compute from the Morse complex of the IVT, and we leverage the empirical observation that most ARs have elongated shapes.
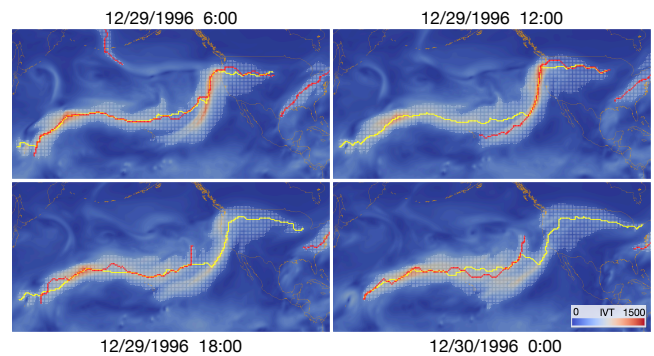

Figure 12: *Comparison between the AR axis computed by Guan and Waslier (red) and our topological axis (yellow).*

In Fig. 12, we show the AR regions by `guan_waliser_v3` in white, the associated AR axes in red, and our topological axes in yellow. There are four consecutive time steps, with 6-hour intervals. In the first time step, `guan_waliser_v3` identifies an AR axis that spans the entire length of the AR region. Our topological method identifies a similar axis with few discrepancies. However, as we move forward in time, the AR axes from `guan_waliser_v3` fail to cover the entire AR region and have inconsistent locations. In contrast, our topological axes consistently span the entire region of the ARs. The advantage of our topological axes is that after persistence simplification, features with less persistence, hence less important in the axis computation, are removed from our topological skeletons. Compared to the local search method by `guan_waliser_v3`, we are less likely to be stuck in local maxima and deviate from the main axis of the AR.

7. Expert Feedback

Throughout the development of our framework, we regularly consulted climate scientists from a national laboratory, who provided valuable insights regarding the usability of the visualization and the analysis of AR events using these visualizations. To formally evaluate our methods, we conducted a series of 45-60 minute interviews with five AR scientists. All experts are either research scientists (E1-E4) at national laboratories or professors (E5) at research universities in the department of earth and atmospheric sciences. All experts are knowledgeable about ARs and have publications on AR-related processes. They all have extensive experience using visualizations in their climate research, although their experiences in designing new visualization techniques vary, ranging from no experience to expert level. We ensured that the experts had a sufficient understanding of our visualization framework by including a thorough introduction to our uncertainty visualization techniques. The interviews commenced with a tutorial on contour boxplots and MetroSets, followed by a case study presentation of the January 7-9, 2017 AR event. Scientists were then invited to offer feedback on the framework's usability, utility, and future potential.

Overall, we received overwhelmingly positive feedback. All experts agreed that the MetroSets was "super intuitive", especially after seeing an example of a train map. E1 commented that for anyone familiar with the map of the trains, MetroSets is easy to understand. In contrast, the contour boxplot was "novel" but more difficult to understand because the 75th percentile could contain smaller boundaries than the 50th percentile. E4 commented that *"it took me a while to understand what is being plotted. But after I understand it, it is a very useful visualization"*. Other experts agreed with E4. E3 added that the contour boxplots and the MetroSets complement each other and are more informative when used together.

For the utility of the visualizations, experts agreed that the contour boxplot provides a useful statistical view, especially as time progresses. E1 said that the contour boxplot helps display the *"spatial extent"* of the AR. Combined with the boundary plot, researchers can determine *"immediately which ARs conform to the traditional shape definition and which ones do not"*. E2 commented that it *"highlights high agreement areas and it provides more information than the overlapping boundary plot"*. For the MetroSets, experts appreciated its simple visual effect without clutter, which facilitates an efficient analysis process. E1 commented that the user *"can get a lot of information in a short amount of time"*. Emphasizing the thick orange edge where the ARDTs agree, E3, E4, and E5 all commented that the MetroSets brought more clarity to *"the core of the AR"*. Some experts expressed interest in the AR's landfall location. E3 noted *"we can see where the AR made landfall with many of the ARDTs, which is incredible"*. E5 added that *"it also helps highlight the disagreements after the AR made landfall and reached more inland"*. On a higher level, E4 remarked that the MetroSets visualization *"goes a step further than computing the boudaries; it gives insights to the inner structure of the AR"*.

Regarding potential improvements, E3 suggested that we could experiment with the combination and ordering of the color palette for MetroSets. This could help improve the contrast and readability of the visualization. The case study presentation to the experts also inspired discussions of various future research directions. E4 pro-

posed a climatological study on ARDTs using contour boxplots. E5 raised the question of whether the 50th percentile band in the contour boxplot differs systematically within an AR's life cycle. Beyond the analysis of past ARs, both E3 and E4 mentioned the potential applications in AR prediction, especially the uncertainty forecasting of the "core", the landfalling location, and the AR impact. E4 also proposed to define a metric for the topological skeletons. The metric would enable a quantitative comparison among the ARDTs, and could potentially improve the current AR tracking algorithms. Along a similar line, E5 suggested the idea of computing a composite or an average of an AR using the MetroSets.

We concluded each expert interview on a positive note, with experts putting forward potentially impactful research questions and suggesting possible solutions using our visualizations. E3 praised the project effort as a whole, saying *"many atmospheric scientists are not necessarily trained in data visualization...there are papers with incredible findings that can be communicated much more clearly by a really good visualization"*.

8. Conclusion and Discussion

We propose two uncertainty visualization techniques to facilitate the analysis of an ensemble of ARs generated by a set of ARDTs. The contour boxplot [WMK13] offers a statistical overview of the AR boundary variations, whereas the MetroSets [JWKN21] inspired visualization of topological skeletons provides a detailed view on the interior structure of the ensemble members. We presented case studies to demonstrate that our visualizations help scientists gain more confidence in their scientific discoveries.

Nevertheless, our methods have limitations. One main shortcoming of the MetroSets is that the topological skeletons are not always faithful to the shapes of the underlying IVT field. There is a trade-off between clarity and faithfulness. A higher simplification threshold on the IVT field offers more clarity by displaying fewer features, but straightening may cause the skeleton to deviate from the IVT's gradient direction. Conversely, a lower threshold with more details leads to better alignment between the MetroSets and the shape of the AR region, but may cause visual clutter. An appropriate persistence threshold is typically selected using a persistence graph [BMS*15], where a plateau in the persistence graph indicates a stable range of scales to separate noise from features. Automating the selection process could be an interesting future direction.

Despite these limitations, our visualizations have proven valuable in assisting climate scientists with the analysis of ARDTs. This objective also aligns seamlessly with the objectives of ARTMIP. For future directions, we will incorporate more ARDT catalogs and integrate our uncertainty visualization framework into an interactive tool for climate scientists to explore or expand our framework to other ensemble simulations.

References

[AMY*22] ATHAWALE T. M., MALJOVEC D., YAN L., JOHNSON C. R., PASCUCCI V., WANG B.: Uncertainty visualization of 2D Morse complex ensembles using statistical summary maps. *IEEE Transactions on Visualization and Computer Graphics (TVCG) 28*, 4 (2022), 1955–1966. doi:10.1109/TVCG.2020.3022359. 2

[BLLS17] BISWAS A., LIN G., LIU X., SHEN H.-W.: Visualization of time-varying weather ensembles across multiple resolutions. *IEEE Transactions on Visualization and Computer Graphics (TVCG) 23*, 1 (2017), 841–850. doi:10.1109/TVCG.2016.2598869. 2

[BMS*15] BREMER P.-T., MALJOVEC D., SAHA A., WANG B., GAFFNEY J., SPEARS B. K., PASCUCCI V.: ND2AV: N-dimensional data analysis and visualization – analysis for the national ignition campaign. *Computing and Visualization in Science (CVS) 17*, 1 (2015), 1–18. doi:10.1007/s00791-015-0241-3. 10

[CDMCR21] COBB A., DELLE MONACHE L., CANNON F., RALPH F. M.: Representation of dropsonde-observed atmospheric river conditions in reanalyses. *Geophysical Research Letters 48*, 15 (2021), e2021GL093357. doi:10.1029/2021GL093357. 4

[CLG*18] CHEN X., LEUNG L. R., GAO Y., LIU Y., WIGMOSTA M., RICHMOND M.: Predictability of extreme precipitation in western U.S. watersheds based on atmospheric river occurrence, intensity, and duration. *Geophysical Research Letters 45*, 21 (2018), 11,693–11,701. doi:10.1029/2018GL079831. 3

[CLWR19] CHEN X., LEUNG L. R., WIGMOSTA M., RICHMOND M.: Impact of atmospheric rivers on surface hydrological processes in western U.S. watersheds. *Journal of Geophysical Research: Atmospheres 124*, 16 (2019), 8896–8916. doi:10.1029/2019JD030468. 1

[Det13] DETTINGER M. D.: Atmospheric rivers as drought busters on the U.S. west coast. *Journal of Hydrometeorology 14*, 6 (2013), 1721–1732. doi:10.1175/JHM-D-13-02.1. 1

[DL17] DI LIBERTO T.: Soaking rains and massive snows pile up in California in january 2017. climate.gov, January 2017. URL: https://www.climate.gov/news-features/event-tracker/soaking-rains-and-massive-snows-pile-california-january-2017. 7

[DRD*11] DETTINGER M. D., RALPH F. M., DAS T., NEIMAN P. J., CAYAN D. R.: Atmospheric rivers, floods and the water resources of California. *Water 3*, 2 (2011), 445–478. doi:10.3390/w3020445. 1

[EHZ01] EDELSBRUNNER H., HARER J., ZOMORODIAN A.: Hierarchical Morse complexes for piecewise linear 2-manifolds. In *Proceedings of the 17th Annual Symposium on Computational Geometry* (Medford, MA, USA, 2001), pp. 70–79. doi:10.1007/s00454-003-2926-5. 3

[EKS83] EDELSBRUNNER H., KIRKPATRICK D., SEIDEL R.: On the shape of a set of points in the plane. *IEEE Transactions on Information Theory 29*, 4 (1983), 551–559. doi:10.1109/TIT.1983.1056714. 5

[ELZ00] EDELSBRUNNER H., LETSCHER D., ZOMORODIAN A.: Topological persistence and simplification. In *Proceedings 41st Annual Symposium on Foundations of Computer Science* (2000), pp. 454–463. doi:10.1109/SFCS.2000.892133. 3

[GMS*17] GELARO R., MCCARTY W., SUÁREZ M. J., TODLING R., MOLOD A., TAKACS L., RANDLES C. A., DARMENOV A., BOSILOVICH M. G., REICHLE R., WARGAN K., COY L., CULLATHER R., DRAPER C., AKELLA S., BUCHARD V., CONATY A., DA SILVA A. M., GU W., KIM G.-K., KOSTER R., LUCCHESI R., MERKOVA D., NIELSEN J. E., PARTYKA G., PAWSON S., PUTMAN W., RIENECKER M., SCHUBERT S. D., SIENKIEWICZ M., ZHAO B.: The modern-era retrospective analysis for research and applications, version 2 (MERRA-2). *Journal of Climate 30*, 14 (2017), 5419–5454. doi:10.1175/JCLI-D-16-0758.1. 2, 4

[GW15] GUAN B., WALISER D. E.: Detection of atmospheric rivers: evaluation and application of an algorithm for global studies. *Journal of Geophysical Research: Atmospheres 120*, 24 (2015), 12514–12535. doi:10.1002/2015JD024257. 1, 2

[GW19] GUAN B., WALISER D. E.: Tracking atmospheric rivers globally: spatial distributions and temporal evolution of life cycle characteristics. *Journal of Geophysical Research: Atmospheres 124*, 23 (2019), 12523–12552. doi:10.1029/2019JD031205. 1, 2, 4, 6, 7

[HSSL00] HIGGINS R. W., SCHEMM J.-K. E., SHI W., LEETMAA A.: Extreme precipitation events in the western United States related to tropical forcing. *Journal of Climate 13*, 4 (2000), 793–820. doi:10.1175/1520-0442(2000)013<0793:EPEITW>2.0.CO;2. 1

[IDOZC21] INDA-DÍAZ H. A., O'BRIEN T. A., ZHOU Y., COLLINS W. D.: Constraining and characterizing the size of atmospheric rivers: a perspective independent from the detection algorithm. *Journal of Geophysical Research: Atmospheres 126*, 16 (2021), e2020JD033746. doi:10.1029/2020JD033746. 2

[JWKN21] JACOBSEN B., WALLINGER M., KOBOUROV S., NOLLENBURG M.: MetroSets: visualizing sets as metro maps. *IEEE Transactions on Computer Graphics (TVCG) 27*, 02 (February 2021), 1257–1267. doi:10.1109/TVCG.2020.3030475. 2, 3, 5, 6, 10

[KC22] KIM S., CHIANG J. C. H.: Atmospheric river lifecycle characteristics shaped by synoptic conditions at genesis. *International Journal of Climatology 42*, 1 (2022), 521–538. doi:10.1002/joc.7258. 1

[KDJ*21] KAMAL A., DHAKAL P., JAVAID A. Y., DEVABHAKTUNI V. K., KAUR D., ZAIENTZ J., MARINIER R.: Recent advances and challenges in uncertainty visualization: a survey. *Journal of Visualization* (2021). doi:10.1007/s12650-021-00755-1. 2

[KWN*13] KIM J., WALISER D. E., NEIMAN P. J., GUAN B., RYOO J.-M., WICK G. A.: Effects of atmospheric river landfalls on the cold season precipitation in California. *Climate Dynamics 40*, 1-2 (Jan. 2013), 465–474. doi:10.1007/s00382-012-1322-3. 1

[LPR09] LÓPEZ-PINTADO S., ROMO J.: On the concept of depth for functional data. *Journal of the American Statistical Association 104*, 486 (2009), 718–734. doi:10.1198/jasa.2009.0108. 3

[LSR20] LORA J. M., SHIELDS C. A., RUTZ J. J.: Consensus and disagreement in atmospheric river detection: ARTMIP global catalogues. *Geophysical Research Letters 47*, 20 (2020), e2020GL089302. doi:10.1029/2020GL089302. 2, 3

[MWK14] MIRZARGAR M., WHITAKER R. T., KIRBY R. M.: Curve boxplot: generalization of boxplot for ensembles of curves. *IEEE Transactions on Visualization and Computer Graphics (TVCG) 20*, 12 (2014), 2654–2663. doi:10.1109/TVCG.2014.2346455. 2

[NRW*08] NEIMAN P. J., RALPH F. M., WICK G. A., LUNDQUIST J. D., DETTINGER M. D.: Meteorological characteristics and overland precipitation impacts of atmospheric rivers affecting the west coast of North America based on eight years of SSM/I satellite observations. *Journal of Hydrometeorology 9*, 1 (2008), 22–47. doi:10.1175/2007JHM855.1. 1

[ORL*20] O'BRIEN T. A., RISSER M. D., LORING B., ELBASHANDY A. A., KRISHNAN H., JOHNSON J., PATRICOLA C. M., O'BRIEN J. P., MAHESH A., PRABHAT, ARRIAGA RAMIREZ S., RHOADES A. M., CHARN A., INDA DÍAZ H., COLLINS W. D.: Detection of atmospheric rivers with inline uncertainty quantification: TECA-BARD v1.0.1. *Geoscientific Model Development 13*, 12 (2020), 6131–6148. doi:10.5194/gmd-13-6131-2020. 1, 3

[Pan08] PANG A.: Visualizing uncertainty in natural hazards. In *Risk Assessment, Modeling and Decision Support: Strategic Directions*, Bostrom A., French S., Gottlieb S., (Eds.). Springer Berlin Heidelberg, Berlin, Heidelberg, 2008, pp. 261–294. doi:10.1007/978-3-540-71158-2_12. 2

[PDL*20] PAYNE A. E., DEMORY M.-E., LEUNG L. R., RAMOS A. M., SHIELDS C. A., RUTZ J. J., SILER N., VILLARINI G., HALL A., RALPH F. M.: Responses and impacts of atmospheric rivers to climate change. *Nature Reviews Earth & Environment 1*, 3 (2020), 143–157. doi:10.1038/s43017-020-0030-5. 1

[PRJ12] POTTER K., ROSEN P., JOHNSON C. R.: From quantification to visualization: a taxonomy of uncertainty visualization approaches. In *Uncertainty Quantification in Scientific Computing* (Berlin, Heidelberg, 2012), Dienstfrey A. M., Boisvert R. F., (Eds.), Springer Berlin Heidelberg, pp. 226–249. doi:10.1007/978-3-642-32677-6_15. 2

[PWB*09] POTTER K., WILSON A., BREMER P.-T., WILLIAMS D., DOUTRIAUX C., PASCUCCI V., JOHNSON C. R.: Ensemble-Vis: A framework for the statistical visualization of ensemble data. In *2009 IEEE International Conference on Data Mining Workshops* (2009), pp. 233–240. doi:10.1109/ICDMW.2009.55. 2

[PWL*97] PANG A. T., WITTENBRINK C. M., LODHA S. K., ET AL.: Approaches to uncertainty visualization. *The Visual Computer 13*, 8 (1997), 370–390. doi:10.1007/s003710050111. 2

[RDC*18] RALPH F. M., DETTINGER M. D., CAIRNS M. M., GALARNEAU T. J., EYLANDER J.: Defining "atmospheric river": how the glossary of meteorology helped resolve a debate. *Bulletin of the American Meteorological Society 99*, 4 (2018), 837–839. doi:10.1175/BAMS-D-17-0157.1. 1

[RKLS20] REID K. J., KING A. D., LANE T. P., SHORT E.: The sensitivity of atmospheric river identification to integrated water vapor transport threshold, resolution, and regridding method. *Journal of Geophysical Research: Atmospheres 125*, 20 (2020). doi:10.1029/2020JD032897. 1

[RRC*19] RALPH F. M., RUTZ J. J., CORDEIRA J. M., DETTINGER M., ANDERSON M., REYNOLDS D., SCHICK L. J., SMALLCOMB C.: A scale to characterize the strength and impacts of atmospheric rivers. *Bulletin of the American Meteorological Society 100*, 2 (2019), 269–289. doi:10.1175/BAMS-D-18-0023.1. 6

[RSL*19] RUTZ J. J., SHIELDS C. A., LORA J. M., PAYNE A. E., GUAN B., ULLRICH P., O'BRIEN T., LEUNG L. R., RALPH F. M., WEHNER M., BRANDS S., COLLOW A., GOLDENSON N., GORODETSKAYA I., GRIFFITH H., KASHINATH K., KAWZENUK B., KRISHNAN H., KURLIN V., LAVERS D., MAGNUSDOTTIR G., MAHONEY K., MCCLENNY E., MUSZYNSKI G., NGUYEN P. D., PRABHAT M., QIAN Y., RAMOS A. M., SARANGI C., SELLARS S., SHULGINA T., TOME R., WALISER D., WALTON D., WICK G., WILSON A. M., VIALE M.: The atmospheric river tracking method intercomparison project (ARTMIP): quantifying uncertainties in atmospheric river climatology. *Journal of Geophysical Research: Atmospheres 124*, 24 (2019), 13777–13802. doi:10.1029/2019JD030936. 1, 2, 3, 4, 8

[RSR14] RUTZ J. J., STEENBURGH W. J., RALPH F. M.: Climatological characteristics of atmospheric rivers and their inland penetration over the western United States. *Monthly Weather Review 142*, 2 (2014), 905–921. doi:10.1175/MWR-D-13-00168.1. 1

[RWS*18] RALPH F. M., WILSON A. M., SHULGINA T., KAWZENUK B., SELLARS S., RUTZ J. J., ASGARI LAMJIRI M., BARNES E. A., GERSHUNOV A., GUAN B., OSBORNE T. C., WICK G. A.: ARTMIP-early start comparison of atmospheric river detection tools: how many atmospheric rivers hit northern California's Russian river watershed? In *AGU Fall Meeting Abstracts* (Dec. 2018), vol. 2018, pp. A23H–2938. doi:10.1007/s00382-018-4427-5. 3

[SK16] SHIELDS C. A., KIEHL J. T.: Atmospheric river landfall-latitude changes in future climate simulations. *Geophysical Research Letters 43*, 16 (2016), 8775–8782. doi:10.1002/2016GL070470. 1

[SWMC*22] SHIELDS C. A., WILLE J. D., MARQUARDT COLLOW A. B., MACLENNAN M., GORODETSKAYA I. V.: Evaluating uncertainty and modes of variability for antarctic atmospheric rivers. *Geophysical Research Letters 49*, 16 (2022). doi:10.1029/2022GL099577. 3

[SZD*10] SANYAL J., ZHANG S., DYER J., MERCER A., AMBURN P., MOORHEAD R.: Noodles: a tool for visualization of numerical weather model ensemble uncertainty. *IEEE Transactions on Visualization and Computer Graphics (TVCG) 16*, 6 (2010), 1421–1430. doi:10.1109/TVCG.2010.181. 2

[TFL*17] TIERNY J., FAVELIER G., LEVINE J. A., GUEUNET C., MICHAUX M.: The Topology ToolKit. *IEEE Transactions on Visualization and Computer Graphics (TVCG)* (2017). https://topology-tool-kit.github.io/. 5

[WBCL18] WEN Y., BEHRANGI A., CHEN H., LAMBRIGTSEN B.: How well were the early 2017 California atmospheric river precipitation events captured by satellite products and ground-based radars? *Quarterly Journal of the Royal Meteorological Society 144*, S1 (2018), 344–359. doi:10.1002/qj.3253. 7

[WG17] WALISER D., GUAN B.: Extreme winds and precipitation during landfall of atmospheric rivers. *Nature Geoscience 10*, 3 (Feb. 2017), 179–183. doi:10.1038/ngeo2894. 1

[WHLS19] WANG J., HAZARIKA S., LI C., SHEN H.-W.: Visualization and visual analysis of ensemble data: a survey. *IEEE Transactions on Visualization and Computer Graphics (TVCG) 25*, 9 (2019), 2853–2872. doi:10.1109/TVCG.2018.2853721. 2

[WMK13] WHITAKER R. T., MIRZARGAR M., KIRBY R. M.: Contour boxplots: a method for characterizing uncertainty in feature sets from simulation ensembles. *IEEE Transactions on Visualization and Computer Graphics (TVCG) 19*, 12 (2013), 2713–2722. doi:10.1109/TVCG.2013.143. 2, 3, 10

[WNR13] WICK G. A., NEIMAN P. J., RALPH F. M.: Description and validation of an automated objective technique for identification and characterization of the integrated water vapor signature of atmospheric rivers. *IEEE Transactions on Geoscience and Remote Sensing 51*, 4 (2013), 2166–2176. doi:10.1109/TGRS.2012.2211024. 2, 4, 6

[YWM*20] YAN L., WANG Y., MUNCH E., GASPAROVIC E., WANG B.: A structural average of labeled merge trees for uncertainty visualization. *IEEE Transactions on Visualization and Computer Graphics (TVCG) 26*, 1 (2020), 832–842. doi:10.1109/TVCG.2019.2934242. 2

[ZCL*21] ZHANG M., CHEN L., LI Q., YUAN X., YONG J.: Uncertainty-oriented ensemble data visualization and exploration using variable spatial spreading. *IEEE Transactions on Visualization and Computer Graphics (TVCG) 27*, 2 (2021), 1808–1818. doi:10.1109/TVCG.2020.3030377. 2

[ZN98] ZHU Y., NEWELL R. E.: A proposed algorithm for moisture fluxes from atmospheric rivers. *Monthly Weather Review 126*, 3 (1998), 725–735. doi:10.1175/1520-0493(1998)126<0725:APAFMF>2.0.CO;2. 1

[ZOU*21] ZHOU Y., O'BRIEN T. A., ULLRICH P. A., COLLINS W. D., PATRICOLA C. M., RHOADES A. M.: Uncertainties in atmospheric river lifecycles by detection algorithms: climatology and variability. *Journal of Geophysical Research: Atmospheres 126*, 8 (2021). doi:10.1029/2020JD033711. 3